A Catchment-Based Approach to Modeling Land Surface Processes. Part 2: Parameter Estimation and Model Demonstration

Agnès Ducharne[1], Randal D. Koster[2], Max J. Suarez[3], Marc Stieglitz[4] and Praveen Kumar[5]

May 10, 2000

[1] UMR Sisyphe, Universite de Paris, 75251 Paris cedex 05, France.

[2]Hydrological Sciences Branch, Laboratory for Hydrospheric Processes, NASA/ Goddard Space Flight Center, Greenbelt, MD, USA. (**Corresponding author**)

[3]Climate and Radiation Branch, Laboratory for Atmospheres, NASA/Goddard Space Flight Center, Greenbelt, MD, USA.

[4]Lamont-Doherty Earth Observatory, Columbia University, Palisades, NY, USA.

[5]Dept. of Civil Engineering, University of Illinois, Urbana-Champaign, Illinois, USA.

Abstract

The viability of a new catchment-based land surface model (LSM) developed for use with general circulation models is demonstrated. First, simple empirical functions — tractable enough for operational use in the LSM — are established that faithfully capture the control of topography on the subgrid variability of soil moisture and the surface water budget, as predicted by theory. Next, the full LSM is evaluated offline. Using forcing and validation datasets developed for PILPS Phase 2c, the minimally calibrated model is shown to reproduce observed evaporation and runoff fluxes successfully in the Red-Arkansas River Basin. A complementary idealized study that employs the range of topographic variability seen over North America demonstrates that the simulated surface water budget does vary strongly with topography, which can, by itself, induce variations in annual evaporation as high as 20%.

1 Introduction

The motivation behind the land surface model (LSM) presented in the companion paper by Koster et al. (this issue, referred to as Part 1) is the general lack of development of runoff formulations compared to sophisticated state-of-the-art evaporation formulations [*Koster and Milly*, 1997]. In particular, most LSMs for general circulation models (GCMs) strongly emphasize point processes (e.g. canopy structure and resistances to evaporation) and assume soil moisture to be spatially uniform at the GCM scale, the soil being described as a stack of vertical layers. The transfer of moisture between these layers, which has a crucial impact on both baseflow and overland flow production, is then computed one-dimensionally along the vertical. This point-process focus neglects the critical effects of the horizontal variability of soil moisture, which is largely imposed by precipitation heterogeneity and the lateral redistribution of moisture following topography.

Part 1 proposes a catchment-based LSM for GCMs that accounts explicitly for the control of topography on the small-scale variability of soil moisture and its effects on evaporation and runoff. This LSM, which follows on recent advances in macroscale catchment modeling [*Famiglietti and Wood*, 1994; *Stieglitz et al.*, 1997], recognizes the hydrological catchment as the fundamental land-surface unit. In each catchment, the LSM combines a catchment model describing the redistribution of water according to topography under the effect of gravity with more traditional parameterizations for energy budget processes, namely, vegetation and evaporation parameterizations from the Mosaic LSM [*Koster and Suarez*, 1992; *Koster and Suarez*, 1996], a snow model from *Lynch-Stieglitz* [1994], and a linear soil-heat diffusion scheme.

In the present paper, we examine two critical issues related to the LSM's operational use. First, in Section 2, we determine the extent to which the complex relationships between topography and the surface water budget described in Part 1 can be characterized in terms of empirical functions that are computationally manageable. These functions describe, in particular, the impact of topography on three processes: (1) baseflow, (2) the water transfers between the root zone moisture and the water table, and (3) the lateral distribution of the root zone wetness, crucial to the spatial partitioning of the catchment into three fractions, each representing a distinct hydrological regime and each thereby employing a different treatment of runoff and evaporation. In evaluating these basin-specific empirical functions, we also examine (Section 2.6) the suitability of automated parameter estimation algorithms, which are critical to a global application of the LSM.

The second issue examined in this paper is the success of the LSM in reproducing observed surface fluxes given realistic atmospheric forcing. Such an evaluation is, of course, an essential pre-requisite to the full coupling of the LSM to an atmospheric GCM. Section 3 presents the framework for an offline evaluation study in the Red-Arkansas river basin, adapted from the framework used in the PILPS 2C model intercomparison study [*Wood et al.*, 1998]. The fluxes simulated in this environment with the catchment model are then compared with observational data in section 4. This section also highlights some unique features of the LSM's behavior present in these results, and it presents an additional idealized calculation that very clearly isolates the impact of topographical variations on the surface fluxes.

Together, Sections 2 and 4 serve to demonstrate that the catchment LSM described in Part 1 is more than a set of unconventional but untested ideas — the version of the catchment LSM used herein efficiently captures the effects of topography on the surface water budget and realistically transforms atmospheric forcing variables into surface fluxes. This is emphasized again in section 5, which provides some additional discussion.

2 Topography-related Parameterizations

In this section, the strategy employed to parameterize the three topography-related processes as a function of the catchment moisture and topography is first detailed in the case of a specific catchment, the Sleepers River catchment of Vermont. This strategy is then evaluated across about 5000 catchments spanning North-America.

2.1 The Sleepers River Catchment

The hydrological catchment examined first is sub-catchment W-3 (8.4 km^2) of the Sleepers River Watershed (111 km^2), located in the highlands of Vermont and monitored since 1957 by the Agricultural Research Service (ARS). More details can be found in *Stieglitz et al.* [1997] and *Anderson* [1977]. In particular, the topography of this catchment is described by a 30 m $\times$ 30 m DEM. The topographic index distribution was computed at this resolution [*Stieglitz et al.*, 1997], and the first three moments are given in Table 1.

This table also gives the values used to describe soil properties. The saturated conductivity at the surface $K_s(d = 0)$ was established by Stieglitz et al. (1997) for the Sleepers River catchment, based on the values proposed by *Beven* [1982] for different vegetation cover and soil texture. The parameter ν describing the decay of K_s with depth was also evaluated by Stieglitz et al (1997) for the Sleepers River catchment. The soil matrix potential at saturation ψ_s and the soil parameter b have standard values from *Cosby et al.* [1984].

2.2 Background: Topography and Water Table Depth

The TOPMODEL framework gives an analytical relationship between the local topographic index x (defined as the log of the ratio of contributing area to local slope; see *Beven and Kirkby* [1979]) and the local water table depth d:

$$d = \overline{d} - \frac{1}{\nu}\left(x - \overline{x}\right) \tag{1}$$

where $\overline{x}$ is the mean of the topographic index in the catchment, $\overline{d}$ is the mean water table depth in the catchment, and ν describes the exponential decay of the saturated hydraulic conductivity K_s with depth. Following *Sivapalan et al.* [1987], the actual discrete distribution of the topographic index can be conveniently represented with a three-parameter gamma distribution:

$$f_T(x) = \frac{1}{\Gamma(\phi)\chi}\left(\frac{x-\mu}{\chi}\right)^{\phi-1}\exp^{-\left(\frac{x-\mu}{\chi}\right)}, \quad \chi, \phi > 0 \tag{2}$$

The three parameters are derived from the mean ($\overline{x}$), variance(σ_x^2), and skewness (γ_x) of the actual distribution of the topographic index, so that the gamma distribution has the same first three moments as the actual distribution. This imposes that:

$$\begin{aligned}\chi &= \gamma_x \, \sigma_x / 2 && (3)\\ \phi &= \sigma_x^2 / \chi^2 && (4)\\ \mu &= \overline{x} - \phi\chi && (5)\end{aligned}$$

The resulting three-parameter gamma distribution is displayed in Figure 1a for the Sleepers River catchment. Being analytical, this idealized distribution has the advantage of being much easier to manipulate than the actual discrete distribution. In particular, the combination of (1) and (2) through a variable change leads to an equation for the distribution of the water table depth, given its mean $\overline{d}$:

$$f_D(d) = -\frac{1}{\Gamma(\phi)\chi_D} \left(\frac{d-\mu_D}{\chi_D}\right)^{\phi-1} \exp^{-\left(\frac{d-\mu_D}{\chi_D}\right)} \qquad (6)$$

with $\chi_D = -\chi/\nu$ and $\mu_D = \overline{d} + (\overline{x} - \mu)/\nu$. This distribution, which is reversed compared to the gamma distribution of x, is displayed in Figure 1b for four different values of $\overline{d}$. This figure shows that the mean water table depth $\overline{d}$ does not change the shape of the distribution, but just induces a shift along the x-axis. Note that the TOPMODEL framework allows "negative" water table depths; these correspond to a water table virtually above the surface, i.e. to local saturation.

2.3 Mean Water Depth and Baseflow

The catchment deficit M_D, an important prognostic variable of the LSM, is based on the equilibrium profile of soil moisture defined in Part 1 (equation I.4):

$$w(z) = \left(\frac{\psi_s - z}{\psi_s}\right)^{-\frac{1}{b}}, \tag{7}$$

where w is the degree of saturation (or "wetness") at a height z above the water table, ψ_s is the matric potential in the soil at saturation, and b is a soil parameter. M_D results from the three-dimensional integration of $1 - w(z)$, first vertically from the ground surface to the local water table depth d, and then laterally over the catchment's distribution of d. The mean water table depth, $\overline{d}$, directly controls the baseflow production, G, via:

$$G = \frac{K_s(\text{surface})}{\nu} e^{-\overline{x}-\nu\overline{d}}, \tag{8}$$

where K_s(surface) represents the surface saturated hydraulic conductivity (see section 3.8 of Part 1).

To relate baseflow production to M_D, we thus employ the intrinsic one-to-one relationship between M_D and $\overline{d}$. This relationship cannot be written analytically, but it can be numerically evaluated. The solid curve in Figure 3a was hence constructed using 50 values of $\overline{d}$ spaced every 10 cm, from $\overline{d}$=-0.9 m to $\overline{d}$=4 m. In the catchment-based LSM, this theoretical relationship is approximated with a simple analytical function:

$$M_D = A\,(\overline{d} + B)^2 \tag{9}$$

where the parameters A and B implicitly describe the influence of topography on the position of the water table and thus on baseflow. To determine the values of A and B in (9), we fit this equation to the theoretical values of M_D computed for two values of $\overline{d}$, namely $\overline{d}$=0 m and $\overline{d}$=2.5 m. Figure 3a compares the resulting approximate function to the theoretical relationship between M_D and $\overline{d}$. The accuracy of the approximate function is very good for values of $\overline{d} < 2.5$ m. Note that, in any case, M_D has an absolute upper limit, to reflect the existence of bedrock (Part 1); at some point, the growing errors suggested at higher water table depths become irrelevant.

The inversion of this approximate function provides an approximate mean water table depth as a function of the prognostic variable M_D. This depth can then be used to approximate the baseflow G using (8). Figure 3b shows a comparison of this baseflow G computed from M_D with that computed directly from $\overline{d}$. For catchment deficits greater than 100 mm ($\overline{d} \geq$ 0.9 m), both the approximate and theoretical baseflow are smaller than 0.01 mm/h, and the corresponding inaccuracies shall have a negligible incidence on the baseflow modeled in the LSM. For smaller catchment deficits, M_D can be successfully used to estimate G. The largest differences occur at very low catchment deficit ($<$ 10 mm). Both the approximate and theoretical baseflow for this situation are, however, very high ($>$ 10 mm/h), so that the catchment deficit is quickly brought back to larger values. In any case, the TOPMODEL assumptions leading to the baseflow equation are less appropriate at such small values of catchment deficit.

2.4 Spatial Distribution of the Root Zone Wetness

2.4.1 Towards an Approximate Distribution

The spatial distribution of the equilibrium root zone wetness, θ, results from the vertical integration across the root zone of the equilibrium soil moisture profile, $w(z)$, at each point in the catchment. As discussed in Part 1, this distribution, $f(\theta)$, is eventually shifted based on the root zone excess variable M_{rz} to account for departures from equilibrium. The resulting distribution is then used to separate the unit catchment into three subunits representing different hydrological regimes. The discussion in Part 1 (see Appendix A) describes how the partitioning of the catchment proceeds given a specific form for f. The present section describes the more technical problem of defining this functional form in a robust but simple way from the LSM's moisture variables, the topography, and the assumptions underlying TOPMODEL.

At any point in the catchment, the value of θ depends non-linearly on the position of the local water table depth d with respect to both the ground surface and the chosen root zone depth d_{rz}. Under this framework, a tractable analytical form for the probability distribution of θ across the catchment cannot be derived from (6). However, this distribution is uniquely related to $\overline{d}$ (or M_D) for a given catchment topography and d_{rz}, and it can be constructed numerically, as shown in Figure 2a for four different values of $\overline{d}$ in the Sleepers River catchment.

Our strategy is to define an analytical approximation to the distribution of θ, with parameters dependent on the catchment deficit on one hand, and the first three moments of the topographic index on the other. The selected distribution is based on a two-parameter exponential distribution:

$$f(\theta) = \alpha^2(\theta - \theta_0)\exp^{-\alpha(\theta-\theta_0)}, \quad \alpha, \theta_0 > 0 \tag{10}$$

where θ_0 is the minimum value of the distribution, and where α is a shape parameter. The comparison of Figure 2a and 2b indicates that the theoretical root zone wetness distribution is well approximated by a two-parameter exponential distribution, with decreasing α as the catchment deficit decreases.

At very low catchment deficit, however, the theoretical root zone wetness distribution is strongly skewed to the left, and cannot be properly approximated by the two-parameter exponential distribution, which is always skewed to the right. This deficiency is an important concern for the representation of the saturated fraction, $A_{\rm sat}$, which would be poorly represented by the integration of the two-parameter exponential distribution for $\theta \geq 1$. Because of the crucial role of variable $A_{\rm sat}$ in the present LSM, it was decided to define it as a third parameter of the root zone wetness distribution. The complete form for the approximate distribution of the root zone wetness at equilibrium can thus be written:

$$\left\{ \begin{array}{lcl} f_{\rm prox}(\theta) & = & 0\,, \quad\quad 0 < \theta \leq \theta_0 \\ f_{\rm prox}(\theta) & = & A_\times\,(\theta - \theta_0)\,\exp^{-\alpha(\theta-\theta_0)}, \quad \alpha, \theta_0 > 0; \quad \theta_0 < \theta < 1 \\ f_{\rm prox}(1) & = & A_{\rm sat} \end{array} \right. \tag{11}$$

The term $A_\times$ is a scaling factor allowing $\int_0^1 f_{\rm prox}(\theta)\,d\theta = 1$, and is a trivial function of $A_{\rm sat}$, α and θ_0. In particular when $A_{\rm sat} = 0$, $A_\times = 1$ and the distribution $f_{\rm prox}$ is identical to the the two-parameter exponential distribution.

2.4.2 Characterization of the Parameters

The parameterization of the root zone wetness distribution as a function of topography and catchment deficit is therefore reduced to the parameterization of the three parameters θ_0, $A_{\rm sat}$ and α as a function of the topography and catchment deficit. The parameters θ_0 and $A_{\rm sat}$ are easily extracted from theoretical distributions of the root zone wetness, as computed numerically over a broad range of water table depths. Figure 4a and 4b show the dependence of θ_0 and $A_{\rm sat}$ on the catchment deficit M_D, in the Sleepers River catchment. The approximate curves on these figures are described in both cases by the following function:

$$Y(M_D) = Y_\infty + (1 - Y_\infty)\,\frac{1 + AM_D}{1 + BM_D + C{M_D}^2} \tag{12}$$

where Y designates either θ_0 or $A_{\rm sat}$. The parameter Y_∞ describes the position of the horizontal asymptote when $M_D \to \infty$. In a completely dry catchment, there is no saturated fraction, so that Y_∞=0 when $Y = A_{\rm sat}$. Because there always remains some residual moisture in the soil, Y_∞ is, in contrast, positive when $Y = \theta_0$; in this case, we take Y_∞ to be the minimum root zone wetness in the distribution constructed for $\overline{d}$=10 m. For both $A_{\rm sat}$ and θ_0, the other three parameters A, B, and C are established by Gaussian elimination. Figure 4a and 4b show that the resulting approximate functions describe extremely well the variations of θ_0 and $A_{\rm sat}$ with M_D.

As mentioned in section 2.4.1, the two-parameter exponential distribution is an excellent approximation for the actual distribution of the root zone wetness θ for larger values of the catchment deficit. The parameter α can then be estimated from θ_{mod}, the location of the first mode (densest value) of the theoretical distribution:

$$\alpha = \frac{1}{\theta_0 - \theta_{\mathrm{mod}}} \tag{13}$$

On the other hand, it is not possible to derive a meaningful value for α at low catchment deficits, when the three-parameter exponential distribution gives a poor representation of the theoretical distribution of θ. Because this distribution gets flatter, however, as the catchment deficit decreases, we choose to define α as an increasing linear function of the catchment deficit (Figure 4c), defined by:

$$\alpha = A_\alpha\, M_D + B_\alpha \tag{14}$$

The basin-specific parameters A_α and B_α are empirically fitted, as detailed in Appendix A.3.

Figure 5 compares the resulting distribution f_{prox} (from (11)) to the theoretical distribution of the root zone wetness in the Sleepers River catchment. The agreement is excellent at high catchment deficit ($\overline{d} = 2$ and 3 m), and it remains quite adequate even at very low catchment deficit.

2.5 Transfers between Soil Moisture Prognostic Variables

As described in Part 1, the transfer of moisture, ΔM_{rz}, from the root zone excess variable, M_{RZ}, to the catchment deficit, M_D, is computed as:

$$\Delta M_{\mathrm{rz}} = -M_{\mathrm{rz}} \frac{\Delta t}{\tau_1}, \tag{15}$$

where Δt is the time step length. The present section describes the empirical equation employed by the catchment model for the timescale τ_1.

The equation for τ_1 as a function of M_{RZ} and M_D is obtained through offline distributed calculations of subsurface catchment moisture dynamics. In each offline calculation, a highly discretized vertical soil column is initialized with a water table depth, an associated equilibrium soil moisture profile, and a root zone excess. The soil moisture profile then evolves to a new state over the course of 24 hours using a discretization of the Richards equation. For the given one-dimensional initialization, the decrease in the root zone excess over the course of a day is thus precisely determined.

Using the same initial root zone excess, the one-dimensional calculation is repeated for a number of different water table depths. Each calculation produces a daily loss associated with a specific depth. Now consider that a given catchment deficit, M_D, and the topographical characteristics of the catchment examined imply a unique distribution of water depth within the catchment. The daily losses generated in the one-dimensional calculations are integrated over this distribution, resulting in a mean loss per day for the catchment as a whole, a function of M_D and M_{RZ}. τ_1 is taken to be the timescale consistent with this daily loss.

The empirical equation that relates τ_1 to M_{RZ} and M_D is:

$$\tau_1 = e^{(a_{\tau 1} + b_{\tau 1} M_D)}, \tag{16}$$

where $a_{\tau 1}$ and $b_{\tau 1}$ depend on the ratio of M_{RZ} to the total water holding capacity of the root zone. If this ratio exceeds .01, then $a_{\tau 1}$ and $b_{\tau 1}$ are assigned one set of values (determined by fitting to the results of the distributed calculations), and if the ratio is less than -.01, then $a_{\tau 1}$ and $b_{\tau 1}$ are assigned a different set of values. Linear interpolation between these two sets provides $a_{\tau 1}$ and $b_{\tau 1}$ for intermediate values of the ratio. Recall that τ_1 applies to a downward flux (out of the root zone) when M_{RZ} is positive and to a negative flux (into the root zone) when M_{RZ} is negative.

The effectiveness of (16) is illustrated in Figure 6. The solid lines represent the timescales derived directly from the distributed calculations (for the case of the Sleepers River catchment), and the dotted lines represent the timescales derived with (16). The agreement is generally strong, particularly for lower values of M_D. As expected, the timescale increases with increasing catchment deficit and decreasing root zone excess.

As discussed in Part 1, the transfer of moisture from the surface excess variable to the root zone variable proceeds analogously to (15). The calculation of τ_2, the timescale of this moisture transfer, is determined via a one-dimensional calculation. The resulting empirical function used to compute τ_2 operationally has the simple form

$$\tau_2 = \frac{a_{\tau 2}}{(M_{\mathrm{rz}} + b_{\tau 2} M_{\mathrm{se}})^3}, \tag{17}$$

where $a_{\tau 2}$ and $b_{\tau 2}$ are fitted parameters.

2.6 Adequacy of the Method in North America

The above section describes the methods used to estimate the model parameters as a function of the catchment deficit, the influence of topography being taken into account implicitly by the parameter themselves. Given the number of catchments considered in a global application of this LSM, automation of these estimation methods is, of course, essential. In the present section, we address the accuracy of our empirical functions over a wide range of catchments spanning North America, subject to the application of automated parameter estimation.

Note that in this section, accuracy refers simply to agreement with the results of the more complex, physically-based calculations and not to agreement with observations. We must emphasize that the more complex calculations themselves are subject to error in the North America analysis because the physical characteristics of the catchments analyzed (e.g., the soil properties and the high resolution topography) are not fully known. For example, the value of ν in (1) has been established in very few places, and thus for convenience we apply the value applicable to the Sleepers River Watershed to all catchments. The theoretical calculations (and thus the empirical fits) would obviously benefit from increased data availability or, at the very least, from scaling studies that show how effective parameter values obtained from relatively small, well-instrumented catchments apply to the larger, more heterogeneous catchments considered here. Of course, the accuracy of any LSM applied at the continental or global scale is limited by the same problem.

In each of the 5020 catchments covering North-America (Part 1), the topographic index has been computed for every 30-arc-second ($\simeq$ 1 km) pixel, based on the topographic information provided at this resolution by the USGS EROS Data Center. Each resulting distribution of the topographic index was analyzed in terms of its first three moments. Some combinations of moments (e.g. those with negative skew) were not directly amenable to a three-parameter gamma distribution and required a preliminary treatment, as described in appendix A.1. We also used a scale correction on the catchment means of the topographic index (appendix A.2), based on the recent work of *Wolock and McCabe* [2000]. In all catchments, the required parameters were finally estimated by fitting (9), (12) and (14) to the theoretical quantities. The automation of this procedure is detailed in appendix A.3.

At this stage, an important concern for use in the LSM is that the resulting approximate baseflow and root zone wetness distribution are accurate enough, at least relative to the theoretical quantities.

2.6.1 Accuracy of Approximate Baseflow

The accuracy of the approximated baseflow was quantified by computing the Root Mean Square Error (RMSE) between it and its theoretical value (i.e. computed directly from $\overline{d}$). (The baseflows in the RMSE calculation were not weighted by catchment area.) In every catchment, the largest contribution to this RMSE is from the inaccuracies at very small catchment deficit. Because such small M_D are rare in the LSM, the RMSE was only computed for values of baseflow corresponding to $M_D \geq 2$ mm. Note that the minimum M_D attained in most catchments, a function of the local climate, is actually much larger than 2 mm, so that the RMSEs computed here are likely to be significantly overestimated. In other words, the baseflow equation works better than implied by the RMSEs below, since these RMSEs still do not reflect "typical" baseflow rates.

This RMSE was computed in all 5020 catchments in North-America, and was found, in 83% of them, to be smaller than 0.15 mm/h, the value computed in the Sleepers River catchment, where baseflow is very successfully approximated (Figure 3b). The largest RMSE found across North-America is 1.13 mm/h, and Figure 7 shows a comparison of the approximate and theoretical baseflow in the corresponding catchment. Despite large errors at very small catchment deficits, the overall behavior of the approximate baseflow in this "worst case" still closely follows the theoretical behavior, which is ruled by topography. This study shows the baseflow RMSE to be reasonably small in the 5020 catchments, which demonstrates the adequacy of the automated parameter estimation procedure.

2.6.2 Accuracy of Approximate Root Zone Distribution

We focused here on the accuracy of two quantities derived from the root zone wetness distribution and used in the LSM. The first one is the saturated fraction A_{sat} itself, which is used for the areal partitioning of each catchment. The second quantity is the mean root zone wetness in the unsaturated but "unstressed transpiration" fraction, defined as:

$$\overline{\theta_{\mathrm{tr}}} = \int_{\theta_{\mathrm{wilt}}}^{1} \theta f_{\mathrm{prox}}(\theta) d\theta \;\; / \;\; \int_{\theta_{\mathrm{wilt}}}^{1} f_{\mathrm{prox}}(\theta)\, d\theta \tag{18}$$

where θ_{wilt} is the wetness at the wilting point. Figure 4b shows, for the Sleepers River catchment, an excellent agreement between the theoretical and approximate values of the saturated fraction A_{sat}. As for baseflow, the largest errors in A_{sat} occur at very low catchment deficit. Again, these low values being very rare in the LSM framework, the RMSEs of both A_{sat} and $\overline{\theta_{\mathrm{tr}}}$ were computed in all 5020 catchments for values of $M_D > 2$ mm.

This analysis shows a satisfying accuracy of $A_{\rm sat}$ in all catchments: 50% of the catchments have a RMSE smaller than the RMSE of $A_{\rm sat}$ in the Sleepers River catchment (RMS=0.032) where $A_{\rm sat}$ was particularly well approximated (Figure 4b). The largest RMSE for $A_{\rm sat}$ is 0.093, and Figure 8a compares the approximate and theoretical saturated fraction in the corresponding "worst case" catchment. The agreement between the two curves is excellent, despite errors at low values of catchment deficit. In particular, the RMSE drops to 0.010 when the values corresponding to $M_D < 15$ mm are excluded from the RMSE computation.

Figure 8b shows a very satisfying agreement between the approximate and theoretical values of $\overline{\theta_{\rm tr}}$ in a catchment with RMSE = 0.018. This RMSE is exceeded in only 17 % of the catchments, which demonstrates the general accuracy of the approximate $\overline{\theta_{\rm tr}}$. Finally, Figure 8c compares the approximate and theoretical $\overline{\theta_{\rm tr}}$ in the catchment with the highest RMSE, where the underestimation of the approximate $\overline{\theta_{\rm tr}}$ is clearly significant. Still, this degree of inconsistency is the exception rather than the rule, and it is not, in any case, large enough to have a first order effect on the results.

2.6.3 Accuracy of Approximate Transfers

At this time, the automated procedure used to extract the parameter values used in the calculation of τ_1, via (16), has been tested on a much more limited scale. For a variety of randomly sampled topographic conditions, the procedure generates parameters that reproduce the timescales obtained through highly distributed calculations. The success in Figure 6 is typical of that obtained in these tests.

As for the calculation of τ_2, the present version of the model uses the same equation and parameters in every catchment; we assume that moisture transfer between the surface layer and the root zone is not, to first order, strongly affected by the topography. Thus, a test of the automated procedure for estimating the parameters in (17) is not performed.

3 The Offline Testing Framework

The accuracy of an LSM can only be determined through a detailed comparison of its products with observations. However, the testing of an LSM coupled to an atmospheric model can be very difficult if the forcing by the atmospheric model is in error. For instance, GCM-simulated precipitation rates are notoriously inaccurate, and these errors would probably dominate the behavior of the LSM. This explains the widespread use in validation studies of "offline" simulations, for which the atmospheric forcing is derived from observations [*Henderson-Sellers et al.*, 1996; *Shao et al.*, 1994; *Dirmeyer et al.*, 1999].

3.1 Description of the Offline Framework

The offline framework developed over the Red-Arkansas River Basin for the Project for Intercomparison of Land-surface Parameterization Schemes (PILPS) Phase 2c [*Wood et al.*, 1998] was adapted for the catchment-based LSM. Figure 9 compares the boundaries of the Red-Arkansas River Basin in PILPS2c and in our study. The latter are much more realistic, since our unit catchments are extracted from a DEM. In particular, the total area is much closer to the actual area proposed by the USGS (566,196 km^2) in the LSM (area = 571,890 km^2) than in the original PILPS2c framework (area = 608,211 km^2). The figure also illustrates the gain in average resolution, as the average area of the unit catchments (4540 km^2) is about half the average size of the 1°× 1°PILPS2c grid-cells (9970 km^2).

Most forcing variables were provided at the 1°× 1° resolution over the PILPS2c domain (Figure 9). The meteorological forcing, available at a 1-hour resolution for ten years (1979-1988), consists of air temperature and humidity at two meters, surface wind and pressure, precipitation, and downwelling solar and longwave radiation. These variables were interpolated from observational point data from the National Climatic Data Center (NCDC). The vegetation properties (leaf area index, greenness fraction, roughness length and snow-free albedo) are derived from the ISLSCP data set for 1987-1988 at the 1°× 1° resolution [*Sellers et al.*, 1996]. The averages of the 1987 and 1988 monthly values are used; thus, seasonal variations in vegetation properties are included but interannual variations are neglected. Porosity and depth of the soil profile have been interpolated from a 1-km resolution soil data base [*STATSGO*, 1994] to the 1°× 1° resolution. Because of the mismatch between the catchment space and the regular 1°× 1° grid, the above forcing fields have been interpolated to the catchment space. To this end, the intersections between the catchments (defined as polygons) and the grid cells have been computed by triangulation, allowing the simple areal weighting interpolation explained in Part 1.

The vegetation type in each catchment was assumed to be one of the eight surface types used in the Mosaic LSM [*Koster and Suarez*, 1996]. The type represented the most within the catchment's area, as determined from vegetation maps on the ISLSCP dataset, was assumed to cover the catchment uniformly. As for the soil properties not mentioned above, they were taken from Table 1 in all catchments. The catchments examined are a subset of the North American catchments examined in section 2.6. As before, the subcatchment distributions of topographic index were derived from 1 km data, and the means of the index were adjusted according to the scaling equation of *Wolock and McCabe* [2000].

The initial conditions for the LSM were obtained by "spinning up" the model for 1 year (with the forcing from 1979) before running it for the ten years. There is therefore no strong equilibrium constraint on the LSM, and this enhances the comparability between modeled and observational quantities [*Wood et al.*, 1998].

3.2 Runoff and Evaporation Data

Relative to most other frameworks for testing LSMs offline, the "Red-Arkansas" framework is spatially extensive and features a lengthy dataset of flux measurements. This multi-year dataset allows us to assess the interannual variability of the fluxes generated by the LSM. Another interesting feature is the quality of the flux measurements, which include (1) daily naturalized streamflows [*Lohmann et al.*, 1998] at the two downstream gauging stations (Little Rock and Shreveport, see Figure 9), and (2) monthly total evaporation over the entire domain, estimated from 1980 to 1986 through an atmospheric budget analysis using radiosonde data [*Liang et al.*, 1998]. Over the 1980-86 period, the accumulated sum of these two data sets balances very closely the accumulated prescribed precipitation, which demonstrates, under the assumption of minimal long-term soil moisture change, the consistency between these two independent data sets and the forcing data.

A routing scheme was used in PILPS2c [*Lohmann et al.*, 1998] to simulate streamflow from modeled runoff. This scheme, designed to route regularly gridded runoff, cannot be easily applied to the catchment-based LSM's products. Because the delay of the routed runoff's peak relative to the non-routed runoff's peak is only 3 to 5 days (Lohmann, personal communication), we can avoid the routing issue by focusing on the monthly to annual timescales.

4 Numerical Results

4.1 Simulation of Fluxes in the Red-Arkansas

Our comparisons with observations in the Red-Arkansas basin focus mainly on the seasonal cycles of areally-averaged evaporation and runoff. Figures 10ab show that the model reproduces well the mean seasonal cycles of these two quantities. Runoff is overestimated slightly in the fall, and evaporation is underestimated slightly in the summer. These errors are small, though, particularly given that the observations themselves are subject to uncertainty. We must emphasize that the Red-Arkansas results were used to a certain extent in the development of this model; thus, the agreement with observed fluxes does not constitute a model validation. We present Figures 10ab mostly to show that the model, with its current design, can reproduce the observed fluxes without an arbitrary tuning of nebulous model parameters. Indeed, the only parameter that was "tuned" in the exercise was the soil depth associated with the surface excess variable. The chosen value for this depth, 5 cm, is consistent with surface layer thicknesses employed by many modeling groups.

Figures 10cd show that the model reproduces the interannual variations of the mean runoff and evaporation cycles as well. Normalized fluxes are shown this time, for a more stringent test of the model. (In a comparison of unnormalized fluxes, even a poor model could produce realistically high runoff rates in response to high precipitation events.) Monthly runoff, which consists mostly of overland flow (from both the Dunne and Horton mechanisms) and is thus driven mainly by the precipitation signal, is realistically simulated: high and low values occur in the correct months, and the amplitude of the seasonal cycle is realistic. Once again, a tendency to overestimate runoff slightly in late summer and fall is apparent. Possible reasons for this overestimation are: (1) a model deficiency, (2) errors in the runoff observations or the forcing observations (precipitation, radiation, etc.) or (3) an inadequate description of the physical properties of the basin itself. We note that every LSM involved in PILPS2c [*Lohmann et al.*, 1998] produced a higher average runoff for October than for May in this basin, so if a model deficiency is to blame, the deficiency is apparently shared by all of the models.

The high peak for the observed normalized runoff in January 1986 reflects the very small precipitation in that month; the absolute runoff error in that month is thus quite small. For such low values of precipitation (or net radiation, for the evaporation plot), the usefulness of the normalized statistic is greatly reduced. Indeed, low values of precipitation and net radiation explain many of the other "underestimations" of normalized winter runoff and evaporation in the latter half of the simulation period. When absolute values of the simulated and observed fluxes are compared (not shown), the agreeement is quite good – the apparent biases largely disappear.

4.2 Unique Aspects of the Model Behavior

The Red-Arkansas framework allows us to demonstrate original features of the catchment-based LSM's behavior. Figure 11 illustrates the influence of the meteorological conditions on the catchment partitioning, a key aspect of the LSM. The 1980-86 mean precipitation in catchment A, which is in the eastern part of the river basin, is 1246 mm/y, whereas that in catchment B, in the western part, is 635 mm/y. The figure shows that this difference in precipitation leads to different seasonal dynamics of the wilting, transpiration, and saturated areal fractions. In both catchments, the saturated fraction is higher in winter (when precipitation exceeds evaporation) and decreases in summer (when evaporation exceeds precipitation), with a corresponding summer increase in the wilting fraction. In the wet catchment, however, the saturated fraction exceeds 15% in March, and the wilting fraction appears only during summertime. In contrast, the wilting fraction is greater than 30% all year long in the drier catchment, and the saturated fraction there is always very small.

4.3 An Additional, Idealized Calculation

A clearer demonstration of topographic effects is afforded by the topographical description of North American catchments utilized in Section 2. In an idealized experiment, we force all 5020 catchments with the same single time-series of meteorological forcing. All catchments are also given the same surface parameters, such as vegetation type (grassland), leaf area index, and roughness length. Thus, the *only* differences between the catchments are their topographical statistics and their associated fitted functions for hydrological regime separation, baseflow generation, and subsurface moisture transport. By comparing the variations in the fluxes generated by the different catchments, we can get a sense for how important the modeled topographic effects are, given the range of topographical characteristics likely to be encountered in a global simulation.

The simulation is broken up into three time segments. In the first segment, a year of meteorological forcing is applied repetitively until all catchment moisture variables come to equilibrium, i.e., until the variables attain the same values at the end of the year as they have at the beginning. The meteorological forcing data used for this year is the 1987 forcing data for a specific catchment in the Red-Arkansas basin, as derived from the ISLSCP CD-ROM [*Sellers et al.*, 1996]. The same catchment is used to define the surface characteristics of all the catchments in the test. The second time segment is a one-year continuation of the previous simulation, but using the 1988 forcing for the specified Red-Arkansas catchment. The second time segment thus represents a dry year following a relatively wet year (the annual precipitation was 739 mm and 353 mm for 1987 and 1988, respectively). In the third segment, the 1988 forcing data is applied repetitively to bring the catchment moisture variables to a new equilibrium.

Annual values of evaporation and runoff from the three time segments are normalized by the corresponding annual precipitation and plotted against certain topographical statistics in Figure 12. Again, the catchments differ only in their topographical description; thus, if a similar experiment were performed with a standard one-dimensional SVAT model, all catchments would produce precisely the same runoff and evaporation values. Figure 12 shows that differences in topography can lead to significant differences in runoff (up to about 20%). Differences in evaporation can be as high as 5% for the equilibrated years and 20% for the transition year (the second time segment). Note that evaporation exceeds precipitation during this second year; moisture stored during the relatively wet 1987 is evaporated during 1988.

The topographic statistics chosen for plotting are those that correlate best with runoff and evaporation. Runoff correlates best with the skewness of the topographic index. Although baseflow is, of course, highly correlated with the mean of the topographic index, the total runoff for this imposed climate is dominated by overland flow, and the overland flow depends in part on the saturated fraction of the catchment. The skewness helps determine this saturated fraction. Evaporation, on the other hand, correlates best with the standard deviation of the topographic index, presumably because the standard deviation contributes most to the shape of the root zone moisture distribution at the onset of wilting, which in turn determines the dynamics of the wilting fraction, A_{wilt}. Note that the presence of scatter in these plots shows that other statistics (such as the mean) can be important as well.

Figure 12 clearly demonstrates the impact of topographic effects, as modeled, on the annual mean surface water balance. The next logical step, of course, is to validate these topographic effects against observations. The isolation of the topographic effects from all other effects (meteorology, surface characteristics, etc.) in the observational record will be addressed in a future study.

5 Conclusions and Discussions

Many studies have demonstrated the impact of small scale spatial variability in hydrological processes on the average interactions between the land surface and the atmosphere [*e.g. Avissar and Pielke,* 1989, *Johnson et al,* 1993, *Ducharne et al,* 1998]. This impact limits the ability of point-process models to represent large scale hydrological processes realistically. These considerations motivated the development of a new land surface model for GCMs, the basic framework for which is provided in Part 1. This new model calls for the disaggregation of the land surface into a mosaic of hydrological catchments, determined through the analysis of a high resolution DEM. In each catchment, a catchment model describes the redistribution of moisture according to topography under the effect of gravity, based on TOPMODEL [*Beven and Kirkby*, 1979; *Sivapalan et al.*, 1987]. The resulting distribution of the root zone moisture is then used to subdivide the catchment into three fractions, each representing a distinct moisture regime; evaporation and runoff processes are modeled with adapted formulations in each fraction, in order to produce a more accurate estimate of the catchment-mean rates.

Three hydrological processes (baseflow, water transfers in the unsaturated zone, spatial distribution of the root zone moisture) depend on both topography and the bulk catchment moisture in a highly complex way. This paper explains in detail how these processes are approximated by simple, tractable functions of three moisture prognostic variables. Under this framework, the influence of topography is implicitly represented by the parameters of the fitted functions. These functions are pre-processed in every unit catchment, and the approximate relationships are used at each time step in the model, which strongly enhances the performance of the model in terms of memory and CPU requirements. An extensive study amongst the 5020 catchments covering North-America showed that automated procedures produce fitted, empirical functions that capture very well the behavior inherent in the more complex, physically-based calculations. Nevertheless, several improvements can still be brought to the parameter estimation procedure. The fitting of the approximate functions to the theoretical relationships could be optimized, using, for instance, RMSEs as criteria. The chosen form of the fitted functions could perhaps also be improved.

A model using these fitted functions and the other components described in Part 1 has been coded and tested for consistency. This model has then been run offline in the Red-Arkansas River Basin using the framework developed for PILPS2c [*Wood et al.*, 1998]. The overall performance of the catchment-based LSM in this exercise is very satisfactory (Figure 10). Though this does not constitute model validation (indeed, the structure of the model evolved partly as a result of evaluations against these data), the offline simulation does show that the model can accurately reproduce, with a reasonable selection of parameter values and minimal tuning, the observed seasonal and interannual variations in runoff and evaporation.

Note that we cannot use this test to prove that the catchment LSM is superior to the standard SVAT LSM, since a few of the SVAT models had similar success in PILPS2c without any tuning at all. Again, Figure 10 only demonstrates the viability of the catchment LSM in its current form. We nevertheless emphasize, however, that the catchment LSM has important intrinsic, conceptual advantages over the standard SVAT model. Standard SVAT LSMs will always be limited by their one-dimensional treatment of subsurface moisture physics. Though this vertical physics may improve as these models evolve, the one-dimensional framework will always impose a barrier to how well they can perform over large spatial scales. The catchment LSM, on the other hand, has a more physically based, three-dimensional framework, implying that the fluxes it generates are more likely correct for the right reasons. This adds, of course, to one's trust in the model when it is applied in untested locations or under modified climates. In addition, given the three-dimensional framework, the potential for improved performance through model evolution is, arguably, significantly greater for the catchment model. Definitively demonstrating (with observations) that the catchment model performs better than the best SVAT models requires additional measurements over a broader range of time and space scales. This demonstration is reserved for a future study.

The present offline study does demonstrate some unique aspects of the catchment model. Figure 11 shows the dynamic partitioning of the unit hydrological catchments into three sub-fractions. The model simulates in particular the saturated fraction in the unit catchments, and this has important implications for validation, since it is now possible to estimate that quantity through remote-sensing [*Gineste et al.*, 1998; *Franks et al.*, 1998].

An important implication of this study is that evaporation and runoff in a given catchment depend strongly on its topography. This is demonstrated most clearly in Figure 12, which shows, for a dry year following a relatively wet year, topographically-induced variations in annual evaporation spanning 20%. For the particular forcing chosen for this exercise, evaporation appears to be controlled mostly by the standard deviation of the topographic index, whereas surface runoff is controlled mostly by the skew. For forcing that more strongly favors baseflow production, the mean of the topographic index would necessarily be more important.

The general sensitivity of evaporation to topographic statistics in turn has important implications for climate modeling – many studies have demonstrated that the atmospheric general circulation and, in particular, precipitation are sensitive to variations in the surface evaporation rate [e.g., *Shukla and Mintz*, 1982; *Milly and Dunne*, 1994; *Ducharne et al.*, 2000; *Koster et al.*, 2000]. To the degree that these topographic controls are realistic, the use of the catchment LSM in a GCM could, in theory, improve the GCM's simulation of climate.

Many directions can still be explored to improve the realism of this catchment-based LSM. Because the distribution of the topographic index is known to be altered at coarse resolutions [*e.g.*, *Wolock and Price,* 1994; *Zhang and Montgomery,* 1994; *Quinn et al.,* 1995], algorithms to correct the three moments of the topographic index from the effect of the coarse 1-km resolution in GTOPO30 (following for instance the work by *Wolock and McCabe* [2000] used in Appendix A.2), or the use of a finer resolved DEM, are an obvious first direction. We suspect that the model's sensitivity to variations in topography may be enhanced when finer-scale topographical data are considered.

Second, most soil parameters are, in the present incarnation of the model, identical in all catchments but should vary geographically. The value of the TOPMODEL parameter ν, which describes the vertical decay of transmissivity, is particulary difficult to prescribe, since it is not directly measurable. As a first approximation, it could be described as a function of active soil depth. Third, a spatial distribution of the vegetation cover should eventually be introduced in each unit catchment, in order to account for the impact of vegetation heterogeneity on the surface fluxes. Fourth, as mentioned in Part 1, the development of an elevation-based disaggregation scheme for atmospheric forcing, such as precipitation rate or temperature, using the topographical information available for each catchment, should increase the accuracy of the catchment model's outputs.

The list of potential improvements to the model, of course, extends even beyond those just noted. Despite any current shortcomings, though, the model is demonstrated here to be a viable tool for estimating large-scale surface energy and water budgets, a tool that could, with a little work on the interface, be incorporated into a GCM. The fact that the model is not limited by the traditional one-dimensional framework of current LSMs should stand it in good stead as evolving GCMs continue to require more realistic representations of energy and water budgets at the land surface.

A Generation of the Parameters in North America

A.1 Preliminary Treatment of the Topographic Index Distribution

In 110 catchments amid the 5020 covering North-America (2.2 %), the topographic index x has a negative skewness and can therefore not be idealized with a three-parameter gamma distribution (positively skewed). A gamma distribution $f_T(x)$ can however be constructed using the absolute value of the skew. A distribution $f_{T_{\mathrm{neg}}}(x)$, with the same first three moments as the topographic index x, can then be constructed from $f_T(x)$ by symmetry around $\overline{x}$: $f_{T_{\mathrm{neg}}}(x) = f_T(2\,\overline{x} - x)$. The mean and variance are those of $f_T(x)$, and the skew is inversed, and therefore negative, as required.

Another issue is that the gamma distribution is not defined if $\gamma_x = 0$ (eqs. 3, 4). Since this distribution is numerically approximated [*Press et al.*, 1992], very small skewnesses induce numerical problems too, and were therefore modified. Only two catchments have a skewness in the range [-0.005, 0.005]. They were changed to ± 0.005, depending on the sign of the original skewness, and the skew was recomputed, using the variance, to define χ from (3).

Finally, the shape of the gamma distribution for $\phi < 1$ (or skewness > 2), with a vertical asymptote at $x = \mu$ (Figure 13), is not adequate for the numerical construction of neither the root zone wetness distribution nor the relationship between $\overline{d}$ and M_D (9). Because this shape seems, in any case, highly unrealistic for the topographic index, skewnesses were reduced to values smaller than 2 (in absolute value). To prevent numerical problems associated with the shape of the root zone wetness in the case of topographic index distributions that are too sharp, the following adjustments were made:

if γ_x > 1.9 then γ_x = 1.9
if γ_x < -1.6 then γ_x = -1.6

These adjustments addressed 265 catchments(5.3%) in the case of positive skewnesses, and 10 catchments (0.2 %) in the case of negative skewnesses.

A.2 Scale Correction

A number of studies have shown that the distribution of the topographic index is strongly affected by DEM resolution [*e.g.*, *Wolock and Price,* 1994; *Zhang and Montgomery,* 1994; *Quinn et al.*, 1995]. More recently, *Wolock and McCabe* [2000], based on 50 catchments in the conterminous United States, proposed an empirical relationship between the means of the topographic index computed at the 100-meter and 1000-meter (or 30-arc-second) resolutions (mean_{100} and mean_{1000} respectively):

$$\text{mean}_{100} = -1.957 + 0.961 \text{ mean}_{1000} \tag{19}$$

This linear regression explains 93% of the variance of mean_{100}. This correction to the distribution of the topographic index, though limited to the mean, was applied to all 5020 catchments in North-America. The sensitivity of the LSM to this correction is currently under study.

A.3 Automated Parameter Estimation

The different soil characteristics chosen to parameterize baseflow and the root zone wetness distribution in each catchment are, for simplicity, taken from

Table 1. More detailed soil maps [*e.g.*, *STATSGO*, 1994] could, of course, be used to give the parameters a more realistic geographical distribution.

Equation 9, which describes an approximate relationship between M_D and $\overline{d}$, can easily be fitted in all 5020 unit catchments in North-America, using the same approach used in the Sleepers River catchment (section 2.3).

The parameters for A_{sat} and θ_0 (12, 14) are also determined for each of the 5020 catchments in North America. The automated procedure, based on Gaussian elimination in equation (12), requires three points (M_D, Y) for both $Y = A_{\mathrm{sat}}$ and $Y = \theta_0$. In both cases and each catchment, these three points must meet two important requirements: they must describe the whole range of variation of Y, and the resulting second-degree polynomial in denominator in (12) must not have its roots in the range of possible values for M_D.

The automated procedure to estimate α distinguishes two cases according to the value of the skewness γ_x. If $\gamma_x \geq 0.25$, then the dependence of α on M_D is described by a straight line, like in the Sleepers River catchment (14). The determination of the two parameters A_α and B_α requires two points (M_D, α). The first one is (M_D=0, α=1), and the second one is given by the highest considered catchment deficit (for $\overline{d}$=4 m) and the corresponding value of α, using (13). If $\gamma_x < 0.25$, then the dependence of α on M_D is rather described by two joining segments:

$$\text{if } M_D < 100 \text{ mm} \quad \text{then} \quad \alpha = A_1\, M_D + B_1 \tag{20}$$

$$\text{if } M_D \geq 100 \text{ mm} \quad \text{then} \quad \alpha = A_2\, M_D + B_2 \tag{21}$$

The two points used to define A_α and B_α from (14) are kept to define two of the unknowns. The remaining two unknowns are given by the intersection of the two segments, for M_D=100 mm and the corresponding α.

These two segments allow us to account for the fact that, for low or negative skewnesses, the approximate root zone wetness distribution better follows the theoretical distribution if the shape parameter increases at a smaller rate for small values of the catchment deficit.

Acknowledgments

The authors wish to thank Eric Wood, Xu Liang and Dag Lohmann for their help with PILPS2c forcing and validation data. Thanks are also due to Kris Verdin and the EROS Data Center for the characterization of the catchments, to Dave Wolock of USGS for his help with processing the topographic indices, and to Jeff Walker for his analysis of the catchment model's outputs. This work was supported by the Earth Science Enterprise of NASA Headquarters through the EOS Interdisciplinary Science Program and the NASA Seasonal-to-Interannual Prediction Project.

References

Anderson, E., NOAA-ARS cooperative snow reseach project - Watershed hydro-climatology and data for years 1960-1974, *NOAA Tech. Rep. NOAA-S/T 77-2854*, 1977.

Avissar, R., and R. Pielke, A parametrization of heterogeneous land surfaces for atmospheric numerical models and its impact on regional meteorology, *Mon. Weather. Rev., 117*, 2113–2136, 1989.

Beven, K., On subsurface stormflow: An analysis of response times, *Hydrol. Sci. J., 27*, 505–521, 1982.

Beven, K., and Kirkby, M. J., A physically based variable contributing area model of basin hydrology, *Hydrol. Sci. Bull., 24*, 43–69, 1979.

Chen, F. H., Henderson-Sellers, A., Milly, P. C. D., Beljaars, A. C. M., Polcher, J., and 37 others, Cabauw experimental results from the Project for Intercomparison of Land-surface Parameterization Schemes, *J. Climate, 10*, 1194–1215, 1997.

Clapp, R. B., and Hornberger, G. M., Empirical equations for some soil hydraulic properties. *Water Resour. Res., 14(4)*, 601–604, 1978.

Cogley, J., GGHYDRO-Global hydrographic data release 2.0, *Technical Report Trent Climate Note 91-1, Trent University*, 1991.

B. J. Cosby, G. M. Hornberger, R. B. C., and Ginn, T. R., A statistical exploration of the relationships of soil moisture characteristics to the physical properties of soils, *Water Resour. Res., 20(6)*, 682–690, 1984.

Dirmeyer, P., A. Dolman, and N. Sato, The Global Soil Wetness Project: A pilot project for global land surface modeling and validation, *Bull. Am. Met. Soc., 80*, 851–878, 1999.

Ducharne, A., and K. Laval, Influence of the realistic description of soil water-holding capacity on the global water cycle in a GCM *J. Climate*, in press.

Ducharne, A., K. Laval, and J. Polcher, Sensitivity of the hydrological cycle to the parametrization of soil hydrology in a GCM, *Clim. Dyn., 14*, 307–327, 1998.

Famiglietti, J. S., and Wood, E. F., Multiscale modeling of spatially variable water and energy balance processes, *Water Resour. Res., 30*, 3061–3078, 1994.

Franks, S., P. Gineste, K. J. Beven., and P. Merot, On constraining the predictions of a distributed model: The incorporation of fuzzy estimates of saturated areas into the calibration process, *Water Resour. Res., 34*, 787–797, 1998.

Gineste, P., C. Puech, and P. Merot, Radar remote sensing of the source areas from the Coet-Dan catchment, *Hydrol. Process., 12*, 267–284, 1998.

Henderson-Sellers, A., McGuffie, K., and Pitman, A. J., The project for intercomparison of land-surface parametrization schemes (PILPS) : 1992 to 1995, *Clim. Dyn., 12*, 849–859, 1996.

Johnson, K. D., D. Entekhabi, and P. S. Eagleson, The implementation and validation of improved land-surface hydrology in an atmospheric general circulation model, *J. Climate, 6*, 1009–1026, 1993.

Koster, R. D., and Milly, P. C. D., The interplay between transpiration and runoff formulations in land surface schemes used with atmospheric models, *J. Climate, 10*, 1578–1591, 1997.

Koster, R. D., T. Oki and M. Suarez, The offline validation of land surface models: Assessing success at the annual timescale, *Journal of the Meteorological Society of Japan*, 77, 257-263, 1999.

Koster, R. D., Suarez, M., Ducharne, A., Kumar, P., and Stieglitz, M., A catchment-based approach to modeling land surface processes in a GCM - Part I: Model structure, *J. Geophys. Res.*, (this issue), 2000.

Koster, R. D., and Suarez, M. J. , Modeling the land surface boundary in climate models as a composite of independants vegetation stands, *J. Geophys. Res., 97(D3)*, 2697–2715, 1992.

Koster, R. D,. and Suarez, M. J., Energy and water balance calculations in the Mosaic LSM, *NASA Tech. Memo.* 104606, Vol. 9, 1996.

Koster, R. D., M. J. Suarez, and M. Heiser, Variance and predictability of precipitation at seasonal-to-interannual timescales, *J. Hydrometeorology, 1*, 26–46, 2000.

Liang, X., E. Wood, D. Lettenmaier, D. Lohmann, and 23 co-authors, The Project for Intercomparison of Land-surface Parameterization Schemes (PILPS) Phase-2(c) Red-Arkansas River Experiment: 2. Spatial and temporal analysis of energy fluxes, *J. Global and Planetary Change, 19*, 137–159, 1998.

Lohmann, D., D. Lettenmaier, X. Liang, E. Wood, and 23 co-authors, The Project for Intercomparison of Land-surface Parameterization Schemes (PILPS) Phase-2(c) Red-Arkansas River Experiment: 3. Spatial and temporal analysis of water fluxes, *J. Global and Planetary Change, 19*, 161–179, 1998.

Lynch-Stieglitz, M., The development and validation of a simple snow model for the GISS GCM, *J. Climate, 7*, 1842–1855, 1994.

Milly, P. C. D. and K. A. Dunne, Sensitivity of global water cycle to the water holding capacity of land, *J. of Climate*, 7(4), 506-526, 1994.

Oki, T., T. Nishimura, and P. Dirmeyer, Validating land surface models by runoff in major river basins of the globe using Total Runoff Integrating Pathways (TRIP), *J. Meteor. Soc. Japan, 77*, 235–255, 1999.

Press, W., S. Teukolsky, W. Vetterling and B. Flannery, *Numerical Recipes in Fortran 77 - The Art of Scientific Computing - Second Edition.* Cambridge University Press, 1992.

Quinn, P., K. Beven, and R. Lamb, The ln(a/tanB) index: how to calculate it and how to use it within the TOPMODEL framework, *Hydrol. Process., 9*, 161–182, 1995.

Sellers, P., Meeson, B. W., Closs, J., Collatz, J., Corprew, F., Dazlich, D., Hall, F. G., Kerr, Y., Koster, R., Los, S., Mitchell, K., McManus, J., Myers, D., Sun, K. J., and Try, P. , The ISLSCP Inititative I global data sets: surface boundary conditions and atmospheric forcings for land-atmosphere studies, *Bull. Am. Met. Soc.*, 1996.

Shao, Y., Anne, R., Henderson-Sellers, A., Irannejad, P., Thornton, P., Liang, X., Chen, T., Ciret, C., Desborough, C., Balachova, O., Haxeltine, A., and Ducharne, A., Soil moisture simulation. A report of the RICE and PILPS workshop, *IGPO Publications Series*, Number 14, 1994.

Shukla, J. and Y. Mintz, Influence of land-surface evapotranspiration on the earth's climate, *Science*, *215*, 1498-1501, 1982.

Sivapalan, M., Beven, K., and Wood, E. F., On hydrologic similarity : 2. a scaled model of storm runoff production, *Water Resour. Res., 23(12)*, 2266–2278, 1987.

STATSGO, State soil geographic (STATSGO) data base: Data use information, *Technical Report Technical Report 1492, U.S. Dept. Agri*, 1994.

Stieglitz, M., Rind, M., Famiglietti, J., and Rosenzweig, C., . An efficient approach to modeling the topographic control of surface hydrology for regional and global modeling, *J. Climate*, *10*, 118–137, 1997.

Wolock, D. and G. McCabe, Differences in topographic characteristics computed from 100- and 1000-meter resolution digital elevation model data, *Hydrol. Process.*, in press.

Wolock, D. M., and Price, C. V. , Effects of digital elevation model map scale and data resolution on a topography-based watershed model, *Water Resour. Res., 30*, 3041–3052, 1994.

Wood, E., Lettenmaier, D., Liang, X., Lohmann, D., and 22 co-authors, The Project for Intercomparison of Land-surface Parameterization Schemes (PILPS) Phase-2(c) Red-Arkansas River River Experiment: 1. Experiment Description and Summary Intercomparisons, *J. Global and Planetary Change, 19*, 115–135, 1998.

Zhang, W., and Montgomery, D. R., Digital elevation model grid size, landscape representation, and hydrologic simulations, *Water Resour. Res., 30*, 1019–1028, 1994.

Figure 1. (a) Theoretical distribution of the topographic index x for Sleepers River. (b) The distribution of depth to the water table d, for 4 values of the mean water depth, for Sleepers River.

Figure 2. Distribution of the root zone wetness at equilibrium, θ: (a) theoretical distribution for 4 values of the mean water depth in the Sleepers River, (b) two-parameter exponential distribution for $\theta_0 = 0$ and different values of α.

Figure 3. Sleepers River catchment: comparison of the theoretical and approximated (a) catchment deficit M_D (mm) as a function of the mean water table depth $\overline{d}$ (m); (b) baseflow G (mm/h) as a function of the catchment deficit (mm).

Figure 4. Sleepers River catchment: comparison of the theoretical and approximated values of a) θ_0 and b) a_1, as a function of the catchment deficit.

Figure 5. Root zone wetness distribution for four different values of the mean water table depth ($\overline{d}$= 0, 1, 2, and 3 m) in the Sleepers River catchment: comparison of the theoretical and approximated distributions.

Figure 6. Contours showing the timescale τ_1 (hours) as computed from the distributed calculations (solid lines) and the empirical approximation, (6).

Figure 7. Accuracy of approximated baseflow : comparison of theoretical

and approximated baseflow (mm/h), as a function of the catchment deficit M_D (mm), in the unit catchment with the highest RMSE.

Figure 8. Accuracy of approximated root zone wetness distribution: comparison of theoretical and approximated quantities, as a function of the catchment deficit M_D (mm). (a) saturated fraction A_{sat} (-) in the unit catchment with the highest RMSE; (b) $\overline{\theta_{\text{tr}}}$ in a unit catchment with RMSE = 0.018, and (c) $\overline{\theta_{\text{tr}}}$ in the unit catchment with the highest RMSE.

Figure 9. Definition of the "Red-Arkansas" spatial domain in the LSM, with the Arkansas river basin (light grey, 85 unit catchments) upstream of Little Rock (AK) and the Red River basin (dark grey, 41 unit catchments) upstream of Shreveport (LA). The thick perimeter defines the Red-Arkansas domain in PILPS2c, at the 1°× 1° resolution (61 grid-cells).

Figure 10. Comparison of simulated and observational fluxes in the Red-Arkansas Basin in 80-86: mean seasonal cycles of (a) evaporation rate and (b) total runoff (mm/d); monthly ratios of (c) runoff to precipitation and (d) latent heat flux to net radiation (-). The maximum peaks of observational ratios (at 7.46 for LE/Rn, and 1.11 for R/P) are truncated in the figure.

Figure 11. Mean seasonal cycle (80-86) of the saturated, unsaturated but unstressed, and stressed fractions in two unit catchments of the Red-Arkansas Basin: an eastern and humid catchment (A) and a western and dry catchment

(B).

Figure 12. Left: Variation of annual runoff (normalized by annual precipitation) with the skew of the topographic index, for three time segments of an idealized simulation (see text). Right: Variation of annual evaporation (normalized by annual precipitation) as a function of the standard deviation of the topographic index.

Figure 13. Influence of the parameter ϕ on the behavior of the gamma distribution.

Table 1: Sleepers River catchment: description of soil and topography.

	Parameter	Value	Unit
Topographic index			
	Mean $\overline{x}$	7.36	-
	Variance σ_x^2	5.51	-
	Skewness γ_x	1.23	-
Soil properties			
	Saturated hydraulic conductivity $K_s(d=0)$	2.2 10^{-3}	m.s^{-1}
	Transmittivity decay factor ν	3.26	m^{-1}
	Saturated soil matrix potential ψ_s	-0.281	m
	Clapp and Hornberger (1978) b	4	-
	Root zone depth d_{rz}	1	m
	Wetness at the wilting point θ_{wilt}	0.26	-

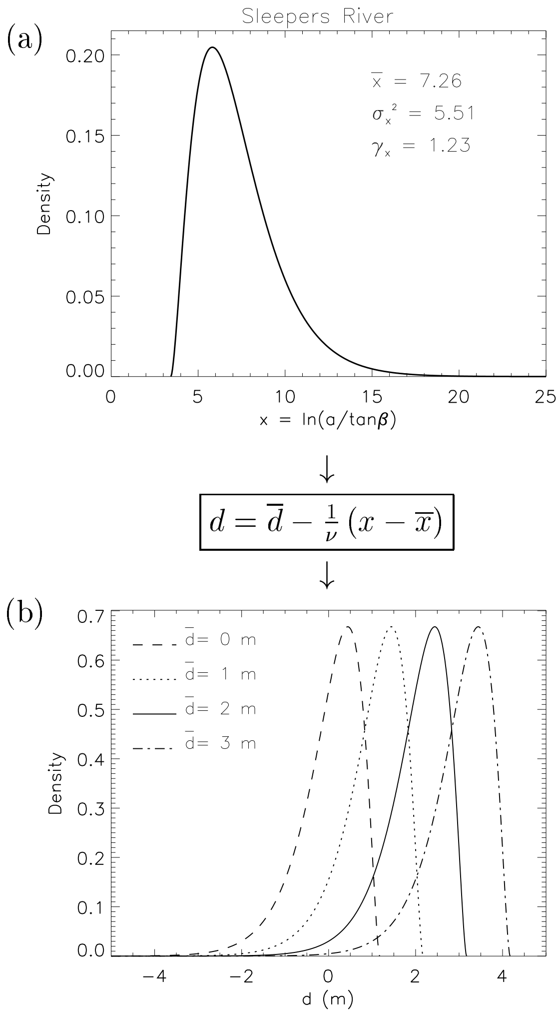

Figure 1: Relationships between (a) the theoretical distribution of the topographic index x, and (b) the distribution of depth to the water table d, for 4 values of the mean water depth, in the case of the Sleepers River.

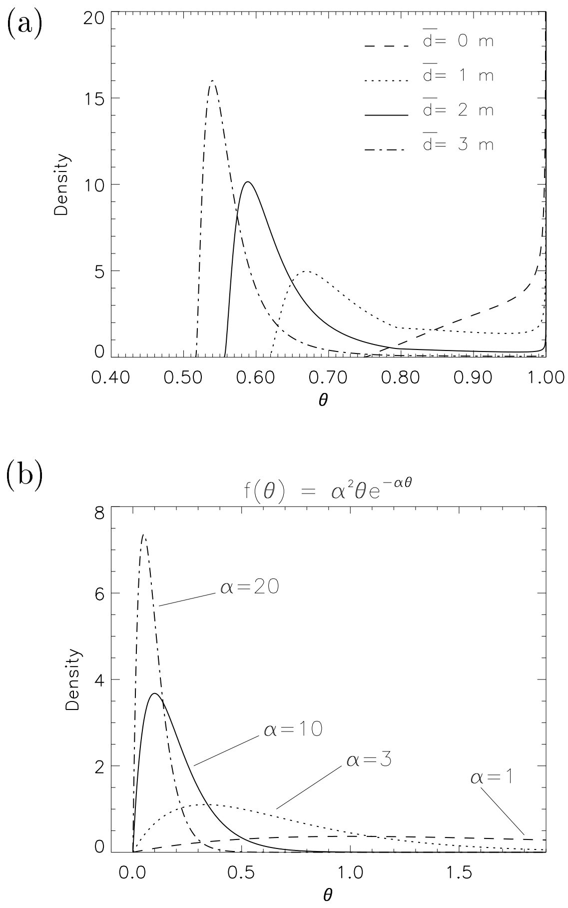

Figure 2: Distribution of the root zone wetness at equilibrium, θ: (a) theoretical distribution for 4 values of the mean water depth in the Sleepers River, (b) two-parameter exponential distribution for $\theta_0 = 0$ and different values of α.

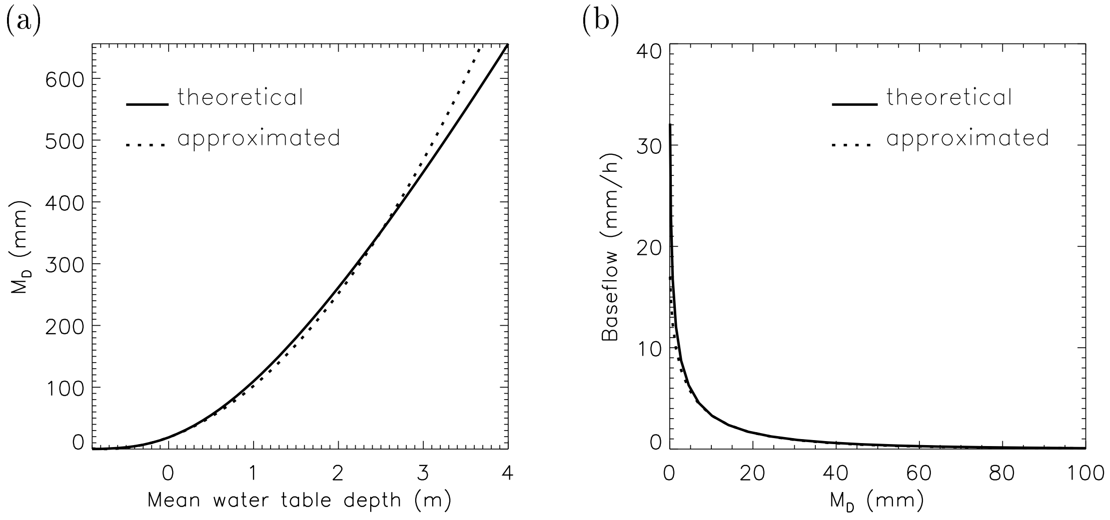

Figure 3: Sleepers River catchment: comparison of the theoretical and approximated (a) catchment deficit M_D (mm) as a function of the mean water table depth $\overline{d}$ (m); (b) baseflow G (mm/h) as a function of the catchment deficit (mm).

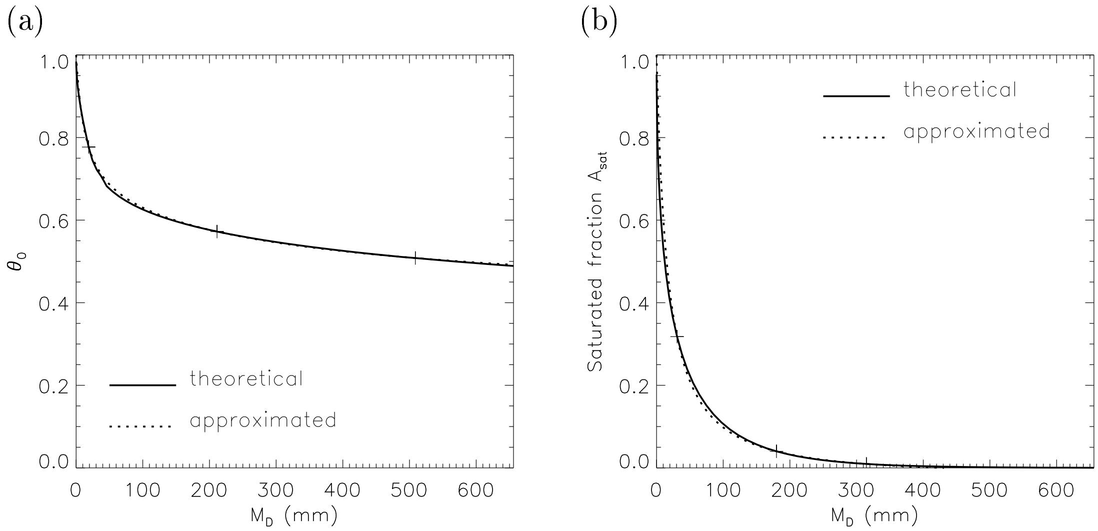

Figure 4: Sleepers River catchment: comparison of the theoretical and approximated values of a) θ_0 and b) a_1, as a function of the catchment deficit.

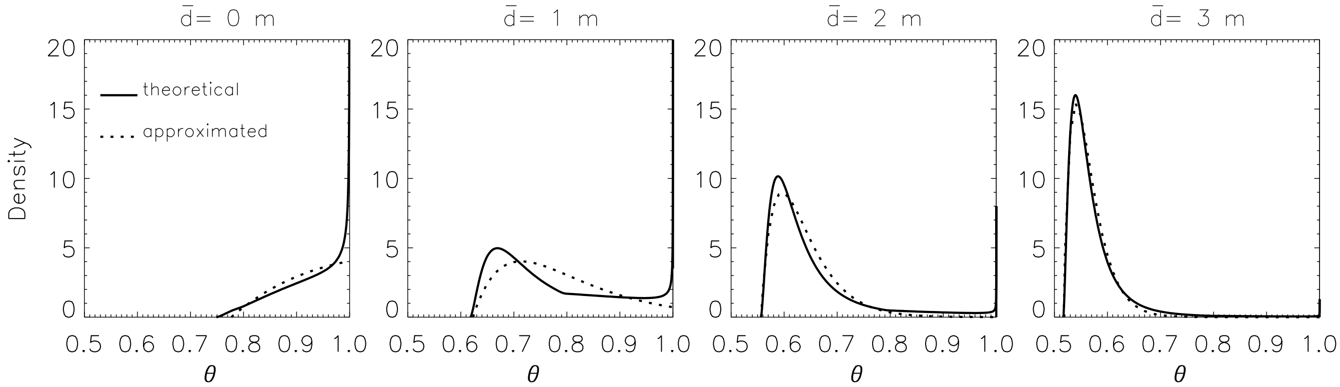

Figure 5: Root zone wetness distribution for four different values of the mean water table depth ($\overline{d}$= 0, 1, 2, and 3 m) in the Sleepers River catchment: comparison of the theoretical and approximated distributions.

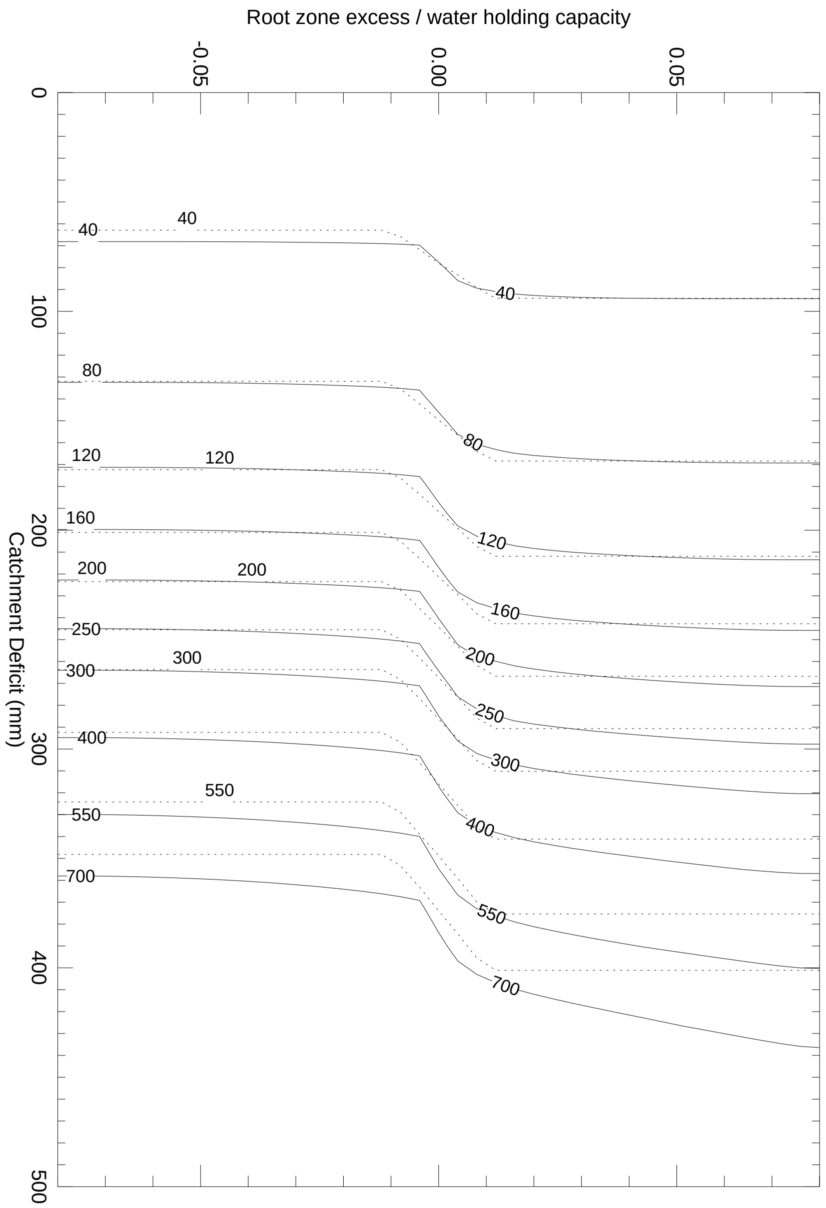

Figure 6: Contours showing the timescale τ_1 (hours) as computed from the distributed calculations (solid lines) and the empirical approximation, (6).

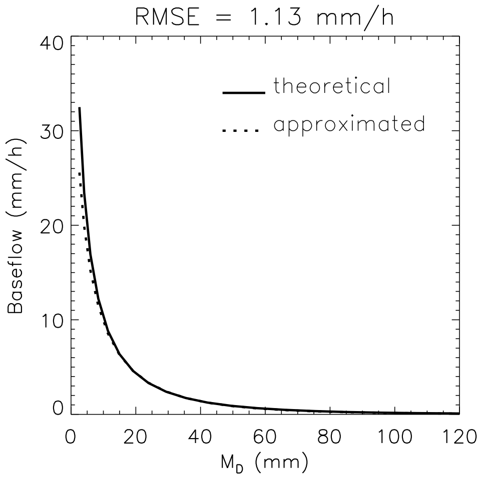

Figure 7: Accuracy of approximated baseflow : comparison of theoretical and approximated baseflow (mm/h), as a function of the catchment deficit M_D (mm), in the unit catchment with the highest RMSE.

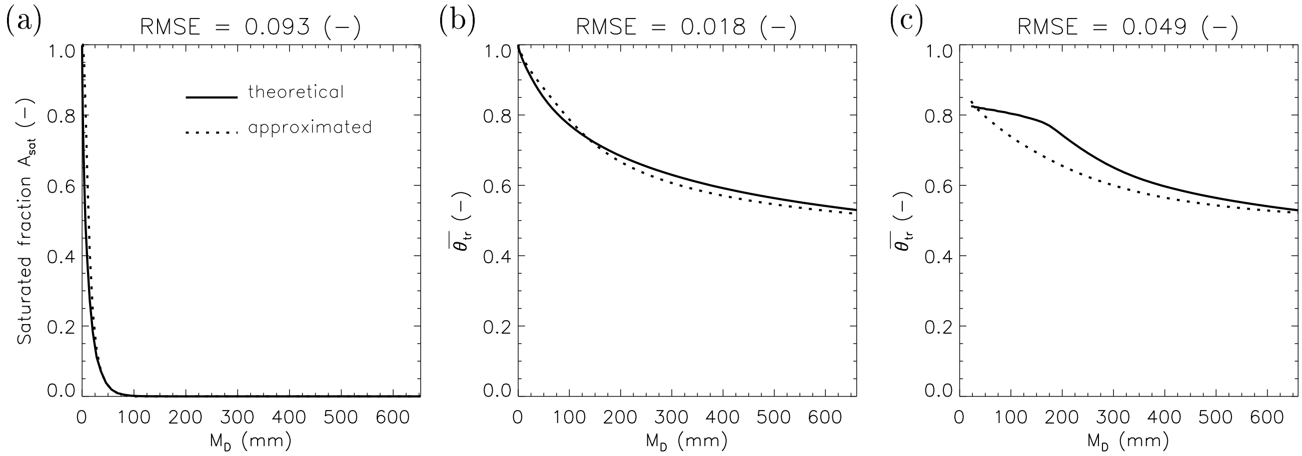

Figure 8: Accuracy of approximated root zone wetness distribution: comparison of theoretical and approximated quantities, as a function of the catchment deficit M_D (mm) : (a) saturated fraction A_{sat} (-) in the unit catchment with the highest RMSE; (b) $\overline{\theta_{\mathrm{tr}}}$ in a unit catchment with RMSE = 0.018, and (c) $\overline{\theta_{\mathrm{tr}}}$ in the unit catchment with the highest RMSE.

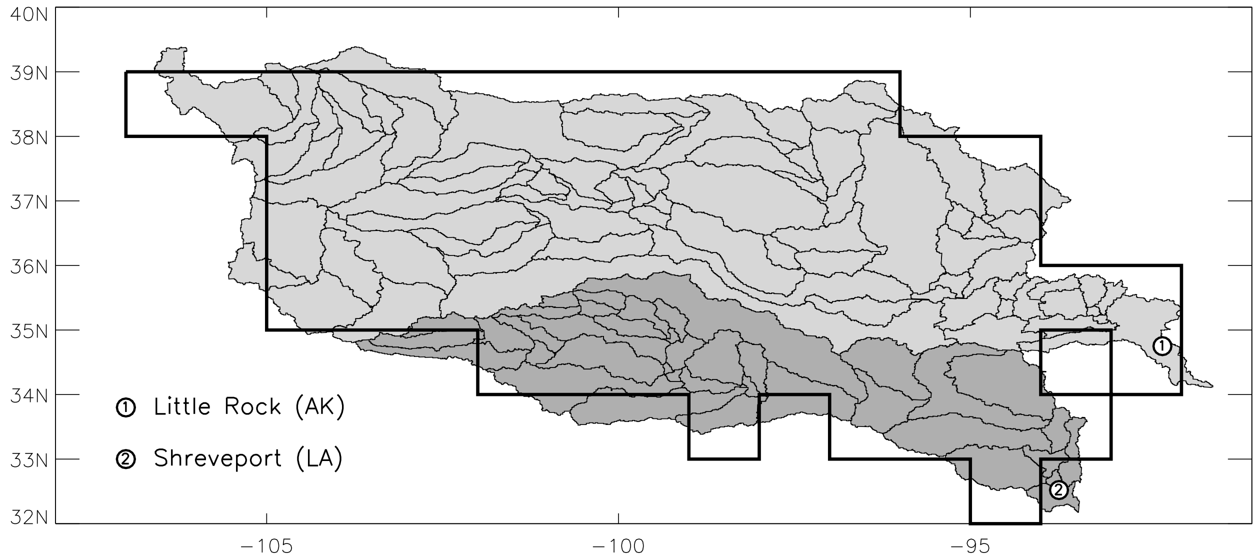

Figure 9: Definition of the "Red-Arkansas" spatial domain in the LSM, with the Arkansas river basin (light grey, 85 unit catchments) upstream of Little Rock (AK) and the Red River basin (dark grey, 41 unit catchments) upstream of Shreveport (LA). The thick regular defines the Red-Arkansas domain in PILPS2c, at the 1°× 1° resolution (61 grid-cells).

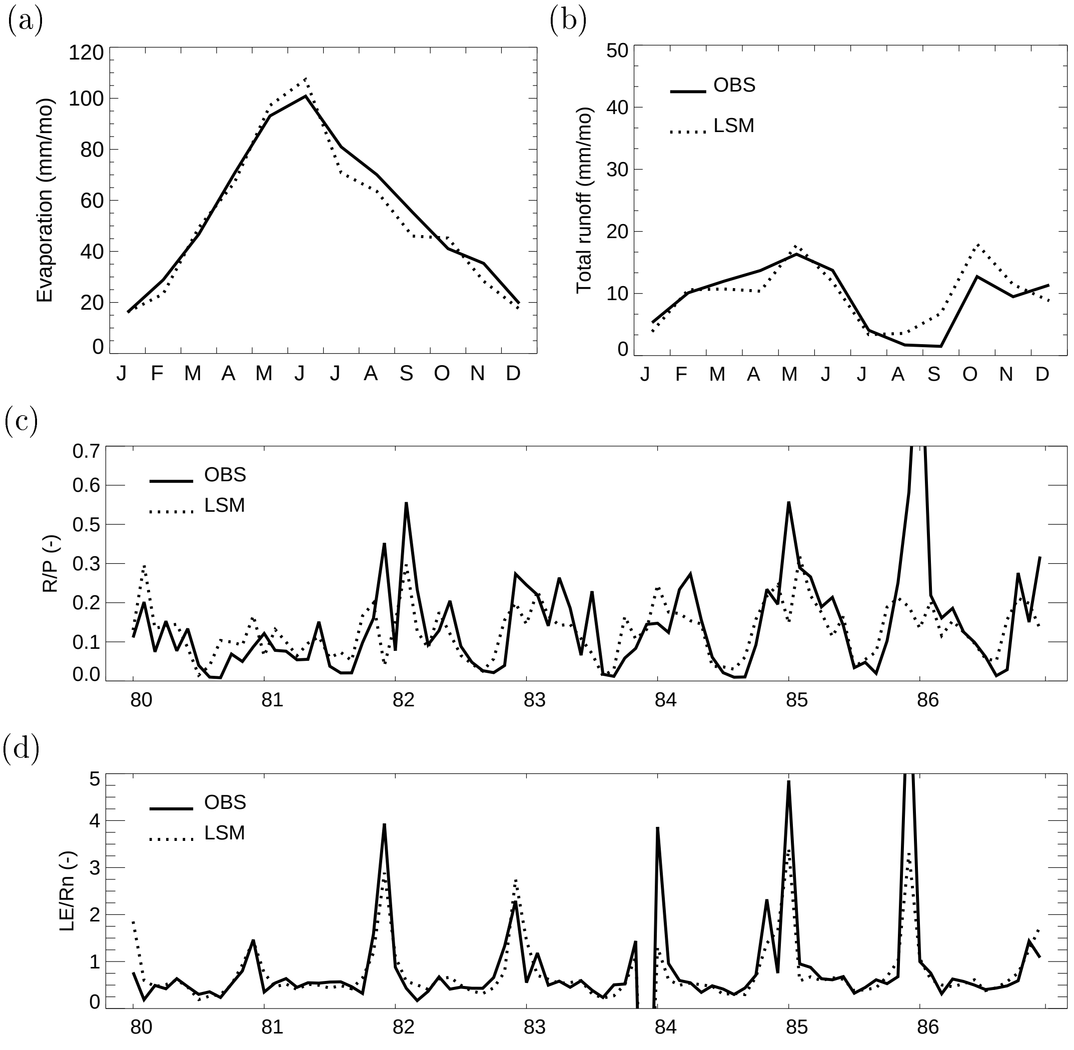

Figure 10: Comparison of simulated and observational fluxes in the Red-Arkansas Basin in 80-86: mean seasonal cycles of (a) evaporation rate and (b) total runoff (mm/d); monthly ratios of (c) runoff to precipitation and (d) latent heat flux to net radiation (-). The maximum peaks of observational ratios (at 7.46 for LE/Rn, and 1.11 for R/P) are truncated in the figure.

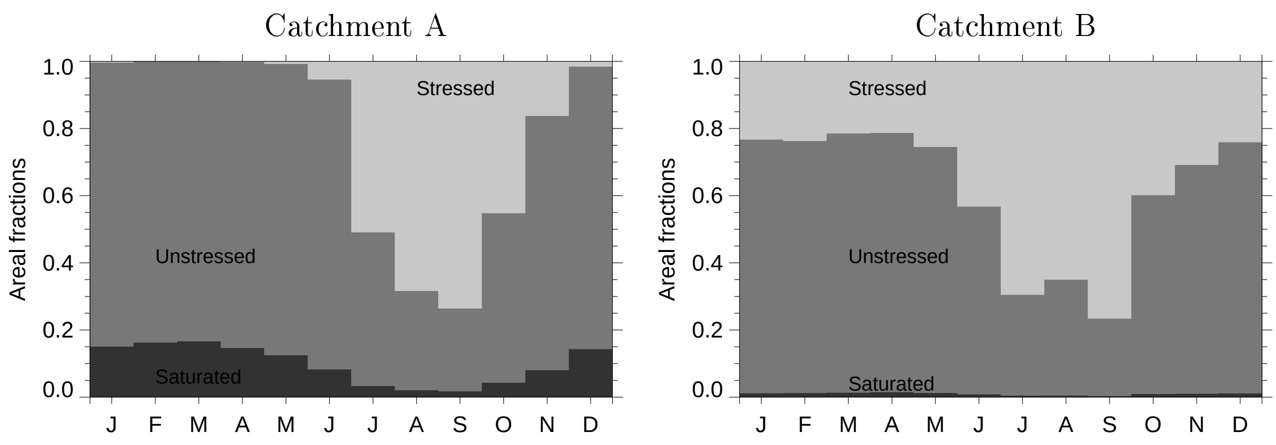

Figure 11: Red-Arkansas Basin: mean seasonal cycle (80-86) of the three catchment's fractions (saturated, unsaturated and unstressed, and stressed fraction) in two unit catchments: A: an eastern and humid catchment, and B: a western and dry catchment.

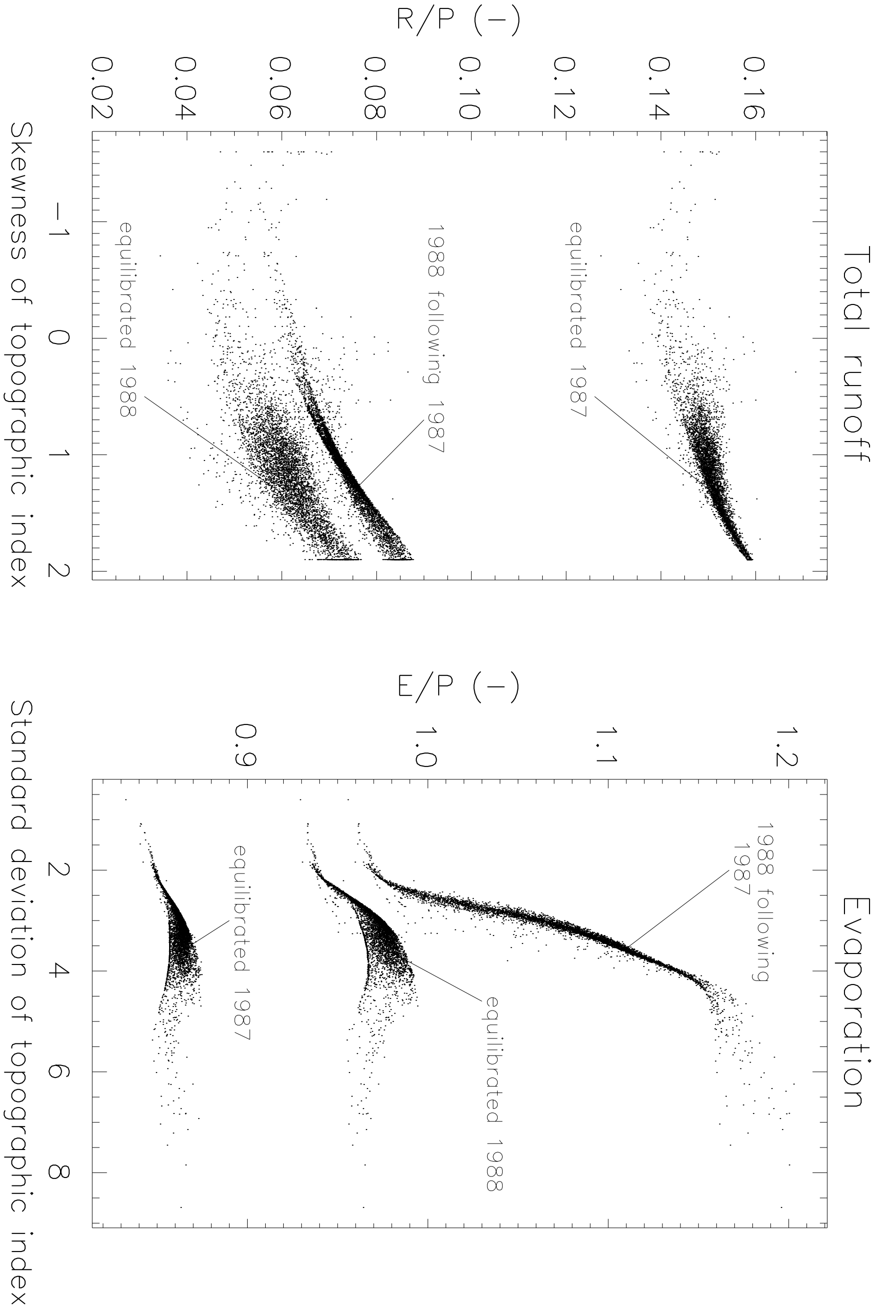

Figure 12: Left: Variation of annual runoff (normalized by annual precipitation with the skew of the topographic index, for three time segments of an idealized simulation (see text). Right: Variation of annual evaporation (normalized by annual precipitation) as a function of the standard deviation of the topographic index.

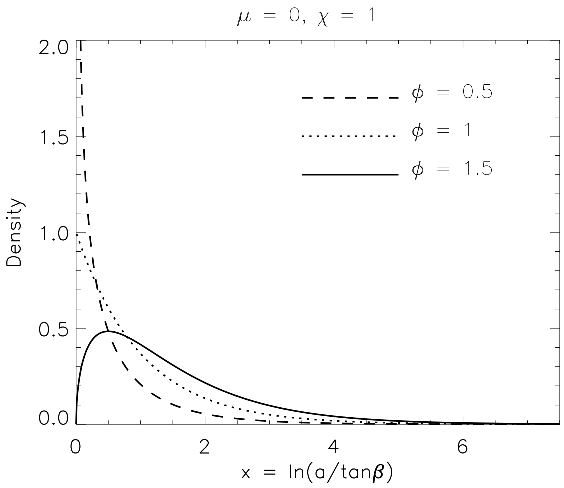

Figure 13: Influence of the parameter ϕ on the behavior of the gamma distribution.